Brain, Behavior, and Immunity 139 (2027) 106962

Contents lists available at ScienceDirect

Brain Behavior and Immunity

journal homepage: www.elsevier.com/locate/ybrbi

Full-length Article

Doxorubicin administration modulates cancer-related fatigue in a time-of-day-dependent manner

Anneke Kastelein [a,1], Ilse R. Kelters [b,c,1], Amy Chin On [d,e], Han Jiao [f,g,h,i], Sonia Martinez Arenas [d], Rico J.E. Derks [j], Elena Sánchez-López [j,k], Anke M. Smits [l], Francesco Angeli [b,m], Marco Guglielmo [b], Joost P.G. Sluijter [b,c], Martin Giera [j,k], Chun-Xia Yi [f,g,h,i], Jacques Neefjes [a], Vasco Sampaio-Pinto [b,c], Laura Kervezee [e], Linda W. van Laake [b,c,*,1], Johanna H. Meijer [d,**,1]

[a] Department of Cell and Chemical Biology, ONCODE Institute, Leiden University Medical Center, 2333 ZC Leiden, the Netherlands
[b] Department of Cardiology and Experimental Cardiology Laboratory, Division of Heart and Lungs, University Medical Centre Utrecht, Utrecht, the Netherlands
[c] Regenerative Medicine Centre Utrecht, Circulatory Health Research Center, University Utrecht, University Medical Centre Utrecht, Utrecht, the Netherlands
[d] Laboratory of Neurophysiology, Department of Cell and Chemical Biology, Leiden University Medical Center, Leiden, the Netherlands
[e] Group of Circadian Medicine, Laboratory for Neurophysiology, Department of Cellular and Chemical Biology, Leiden University Medical Center, Leiden, the Netherlands
[f] Department of Endocrinology and Metabolism, Amsterdam University Medical Center, Location AMC, University of Amsterdam, Amsterdam, the Netherlands
[g] Amsterdam Gastroenterology Endocrinology and Metabolism, Amsterdam, the Netherlands
[h] Department of Clinical Chemistry, Laboratory of Endocrinology, Amsterdam University Medical Center, Location AMC, Amsterdam, the Netherlands
[i] Netherlands Institute for Neuroscience, Amsterdam, the Netherlands
[j] Center for Proteomics and Metabolomics, Leiden University Medical Center, 2300RC Leiden, the Netherlands
[k] The Novo Nordisk Foundation Center for Stem Cell Medicine (reNEW), Leiden University Medical Center, Leiden, the Netherlands
[l] Department of Cell and Chemical Biology, Leiden University Medical Center, 2333 ZC Leiden, the Netherlands
[m] Department of Medical and Surgical Sciences- DIMEC, University of Bologna, Via Giuseppe Massarenti 9, 40138 Bologna, Italy

ARTICLE INFO

Keywords:
Circadian rhythms
Circadian medicine
Chronopharmacology
Cancer-related fatigue
Cancer therapy related cardiac dysfunction
Cancer survivorship
Anthracyclines
Chemotherapy-related adverse effect
Doxorubicin

ABSTRACT

Cancer-related fatigue (CRF) is one of the most debilitating long-term consequences of cancer therapy, with limited treatment options. Anthracyclines, such as doxorubicin (Adriamycin), are cornerstone chemotherapeutics but are associated with substantial toxicity, including fatigue. Notably, doxorubicin has been shown to interfere with the circadian system. Whether the timing of anthracycline administration impacts the development of CRF and other toxicities remains unknown. To investigate this, mice (C57BL/6J) were treated with doxorubicin (4x 5 mg/kg) over a 10-day period at different times of day (ZT2, ZT8, ZT14 or ZT20). Fatigue was assessed by monitoring voluntary running wheel and home-cage locomotor activity. Circadian parameters were derived from running wheel activity. Additionally, cardiac toxicity, neuroinflammation, systemic inflammation, grip strength, body weight, and metabolomic and lipidomic profiles were evaluated.

Doxorubicin treatment at the early active phase (ZT14) elicited the most severe fatigue. This time effect was paralleled by lower plasma cytokines levels, altered metabolomic and lipidomic plasma profiles, and enhanced microglial activity in the suprachiasmatic nucleus (SCN). No parallel time-of day effects were observed in general welfare or cardiac dysfunction. Our results indicate that fatigue severity in mice varies with drug administration time, with fatigue being most severe following treatment at ZT14. The observed increased microglial phagocytic state in the SCN, suggests that the neuroimmune response of this hypothalamic region is critical for developing fatigue. Our findings support the development of time-adjusted anthracycline regimens to improve quality of life of cancer patients and survivors.

* Corresponding author at: Department of Cardiology, Division of Heart & Lungs, University Medical Center Utrecht, Heidelberglaan 100, 3584 CX Utrecht, the Netherlands.
** Corresponding author at: Department of Cell & Chemical Biology, Leiden University Medical Center, Einthovenweg 20, 2333ZC Leiden, the Netherlands.
E-mail addresses: L.w.vanLaake@umcutrecht.nl (L.W. van Laake), j.h.meijer@lumc.nl (J.H. Meijer).
[1] Authors contributed equally.

https://doi.org/10.1016/j.bbi.2026.106962
Received 12 March 2026; Received in revised form 14 August 2026; Accepted 17 August 2026
Available online 20 August 2026
0889-1591/© 2026 The Author(s). Published by Elsevier Inc. This is an open access article under the CC BY license (http://creativecommons.org/licenses/by/4.0/).

1. Introduction

Cancer survival rates have improved substantially over the last decades, shifting the focus of oncology from acute treatment outcomes towards long-term survival and quality of life (Jemal et al., 2017). Many cancer survivors experience adverse effects that may persist for years after completion of treatment. One of the poorly understood consequences of cancer and anticancer treatment is cancer-related fatigue (CRF), affecting approximately 23–49% of long-term cancer survivors (Thong et al., 2020). CRF is a distressing, persistent, and subjective sense of physical, emotional, or cognitive exhaustion that is disproportionate to recent activity, poorly relieved by rest, and that interferes with daily functioning (Berger et al., 2015). Addressing CRF is important, as patients often perceive it as more debilitating than nausea, pain, or depression, with adverse consequences for work productivity, social participation, and overall quality of life (Stone et al., 2000).

Accumulating evidence points to chemotherapy as a major contributor to CRF, independent of cancer type (Goedendorp et al., 2012; de Ligt; Abrahams et al., 2016; Ma et al., 2020). Preclinical studies show that different types of chemotherapy can induce fatigue, with doxorubicin (Adriamycin) having a particularly detrimental effect (Zombeck et al., 2013; Wang et al., 2022). Doxorubicin belongs to the anthracycline drug family and is commonly used to treat a variety of cancers in both adults and children. It exerts its anti-tumour effect through DNA damage, causing double-strand breaks following inhibition of topoisomerase IIα, and chromatin damage, mediated through histone eviction at selected areas in the genome (Tewey et al., 1984; Pang et al., 2013; Qiao et al., 2020). While these mechanisms underlie its potent anticancer efficacy, they also extend to healthy tissues, initiating systemic responses that are recognised as contributing factors in the pathogenesis of CRF. Dysregulation of cytokine signalling, with elevations in IL-6, TNF-related pathways, and IL-1 mediators are observed in patients receiving anthracyclines (Wang et al., 2022; Tometich et al., 2023; Hoogland et al., 2023; Bower and Lamkin, 2013; Santos and Pyter, 2018; Eyob et al., 2016). These inflammatory changes interact with maladaptive hypothalamic–pituitary–adrenal axis activity and impaired glucocorticoid signalling, which may further exacerbate fatigue (Bower et al., 2011). In parallel, microglial activation through pattern-recognition receptors sensing damage-associated molecular patterns contribute to neuroinflammation and blood–brain barrier alterations (Wefel et al., 2015; Rendeiro et al., 2016). Beyond inflammatory effects, doxorubicin induces cardiotoxicity (Fabiani et al., 2025; van der Geest et al., 2025) and circadian disruption (Tapp et al., 2025), both of which may compound fatigue.

Chronopharmacology offers an approach to attenuate treatment related toxicity by adjusting the time of drug administration to the body's circadian rhythms to optimize its efficacy and/or limit adverse effects (Lévi et al., 2024; Bicker et al., 2020). Circadian rhythms are intrinsic biological oscillations of approximately 24 h that allow animals to anticipate and adapt to daily environmental cycles. At the molecular level, circadian rhythms arise from transcriptional–translational feedback loops of core clock genes, which regulate the rhythmic expression of downstream clock-controlled genes in virtually all cells of the body (Patke et al., 2020; Rosensweig and Green, 2020; Schibler et al., 2015). These, in turn, regulate biological processes including metabolism (Lal et al., 2024; Panda, 2016), immune regulation (Wang et al., 2022; Scheiermann et al., 2013), myocardial contractility (Bray et al., 2008; Crnko et al., 2019), and the sleep–wake cycle (Kyriacou and Hastings, 2010). Consequently, circadian regulation of these processes influences therapeutic effects. In patients with high-risk HR+/HER2- early breast cancer, tamoxifen intake in the evening or at night was associated with improved disease-free survival (Giacchetti et al., 2024; Laas et al., 2025), while morning or early afternoon administration of immune checkpoint inhibitors was linked to improved progression-free and overall survival compared with later dosing (Karaboué et al., 2024). In addition, retrospective data indicate that anthracycline-containing regimens administered the afternoon are associated with an increased risk of chemotherapy–induced cardiac dysfunction and heart failure, illustrating the significance of circadian timing in anthracycline cardiotoxicity (Printezi et al., 2025). Whether time-adjusted administration of anthracyclines can reduce CRF is unknown.

We examined whether the time of doxorubicin administration can affect chemotherapy-induced fatigue, considering cardiotoxicity, neuroinflammation and systemic inflammation as potential concurrent adverse effects that may in turn contribute to the CRF phenotype. We treated four groups of non-tumour-bearing mice with doxorubicin at a different time of day and integrated behaviour, physiological, and molecular analyses. Voluntary wheel running activity was used as a robust read-out of fatigue (Zombeck et al., 2013; Wang et al., 2022). Complementary measures included cardiac function, analysis of plasma cytokines, metabolites and lipids, as well as microglial activity and behavioural indicators of circadian disruption. The time-dependent effects of treatment on fatigue allowed us to distinguish general toxic effects of doxorubicin from potential concurrent toxicities contributing to fatigue, thereby providing insight into the primary factors associated with doxorubicin-induced fatigue.

2. Materials and methods

2.1. Ethics statement

All the procedures were conducted in accordance with Dutch Experiments on Animals Act, approved by the Animal Welfare Body Leiden (Leiden, the Netherlands) and the Central Authority for Scientific Procedures on Animals (The Hague, the Netherlands) and conducted under the authority of the Project Licence (1160020185084 and 11600202317590).

2.2. Animals

A total of 142 male and female, 10–12 weeks old C57BL/6J mice were obtained from Envigo (Horst, the Netherlands) and group housed in the animal facility of the Leiden University Medical Center (LUMC, Leiden, The Netherlands) under controlled temperature (20–24°C) and 12:12 h light–dark cycle recording cabinets with *ad libitum* access to food and water. During one week of acclimatisation, animals were housed in type II long cages with standard bedding, a gnawing stick, nesting material, and a carton roll. After acclimatisation, mice were transferred to type III long cages enriched with a vertical running wheel (24 cm diameter), standard bedding, a gnawing stick and nesting material to adapt to the environment and learn wheel running for two weeks. During the treatment phase, mice were individually housed without running wheels, as filter tops, which are incompatible with running wheel use, are required to prevent exposure to excreted doxorubicin. Animals were injected with doxorubicin (4x 5 mg/kg) or vehicle (saline) at Zeitgeber Time (ZT)2, ZT8, ZT14 or ZT20, corresponding to the early light period (ZT2), late light period (ZT8), early dark period (ZT14), and late dark period (ZT20). One week after the final injection, animals were transferred to clean cages with running wheels. To assess general welfare, weight was monitored, and animals were observed for abnormal behaviour, posture and other signs of distress or sickness. Body weight was recorded before the first injection, on each injection day, and the two following days, then weekly after return to running-wheel cages, and immediately prior to termination. The first measurement served as baseline, and consecutive weights were expressed as percentage of baseline. In total, three animals (from ZT2, ZT8 and ZT20) reached a humane endpoint (>20% weight loss) and were removed from the experiment prior to completion. To determine sample size, power calculations were done using running wheel activity data (Wang et al., 2022) with a power of 80% and alpha of 0.05, leading to eight animals per group. All animals were randomly assigned to a treatment and an injection time using the randomization tool Randomice (van Eenige

et al., 2020).

2.3. Reagent preparation and administration

Doxorubicin was obtained from Pharmachemie (Haarlem, The Netherlands) and diluted in sterile 0.9% NaCl (B.Braun Medical NV) to a concentration of 1.5 mg/mL. Mice were weighed and anaesthetised with 4% isoflurane via an induction chamber, after which doxorubicin (5 mg/kg) was administered *retro*-orbitally. The *retro*-orbital route was selected as a less stressful alternative to tail vein injection and is pharmacokinetically comparable to conventional intravenous administration. This corresponded to an injection volume 3.33 μL per gram of body weight. Control mice underwent the same procedure and received 3.33 μL of 0.9% NaCl per gram of body weight. Injections were administered at day 0, 1, 8 and 9, based on our previously published cyclic anthracycline regimen (Wang et al., 2022).

2.4. Time of treatment effects on voluntary running wheel and cage activity

Female mice were single-housed with a running wheel in 12:12 light dark (LD) conditions, as described above. Running wheel and cage activity (the latter measured by a passive infrared sensor) were recorded with ClockLab data collection software (Actimetrics, Illinois, USA) and were stored in 1-min bins. Baseline recordings for the running wheel and cage activity were obtained for two weeks prior to treatment. Following the treatment phase, animals were recorded for two weeks under LD conditions, after which a subset was released in constant darkness (DD) for three weeks to determine the endogenous rhythms in running-wheel and home-cage activity in the absence of external time cues. To assess the post-treatment activity, data was normalised to baseline activity. For each mouse, daily wheel revolutions were expressed as a percentage of its 7-day baseline average. The same was applied to cage activity data. In addition, daily activity patterns during baseline and post-treatment LD and DD were calculated by averaging revolutions and counts per hour over a 7-day period. Circadian locomotor activity variables were derived in Clocklab, including circadian period and strength of the circadian clock using F-periodogram analysis as previously described (Jenni et al., 2006), as well as the non-parametric variables interdaily stability (IS; quantifying synchronisation to the 24 h light–dark cycle), intradaily variability (IV; quantifying rhythm fragmentation) and free running period. To calculate activity onset, offset, alpha duration and phase angle of entrainment, wheel-running data were binned into 10-minute intervals and onset and offset were determined using individually defined activity thresholds (20th and 5th percentile of non-zero counts, respectively). Onset was defined as the first active bin preceded by at least 5 h of inactivity, with at least 30% of the following 5 h being active. Offset was defined as the last active bin from ZT12 onwards followed by at least 95% inactivity over the subsequent 4 h, applied circularly to account for activity past midnight. Alpha duration was calculated as the difference between daily offset and onset times, averaged per animal over baseline (days 8–14) and post-treatment (days 36–42). Phase angle of entrainment was defined as mean onset time relative to lights-off (ZT12), with positive values indicating onset after lights-off. The animals in DD were sacrificed by rapid decapitation under deep isoflurane anaesthesia (4–6%) after 3 weeks in DD. Trunk blood and organs were collected.

2.5. Grip strength

Forelimb grip strength was measured one and three weeks after the final injection using a grid connected to an isometric force transducer (Columbus Instruments, Columbus, OH) as described previously by De Luca (2019). Prior to the analysis, animals were familiarized with the grip strength meter. During the test, animals held the grid with their forepaws and were gently pulled backwards by the tail until they failed to retain the grid, with peak force being automatically recorded. Each mouse performed five trials (five minutes recovery between trials), and the average value was used for analysis.

2.6. Blood collection

Blood samples (≤50 μL) were collected from the lateral tail vein one and three weeks after the final injection. At sacrifice, up to 500 μL trunk blood or cardiac blood was collected in EDTA-coated tubes. Samples were kept on ice until centrifugation at 2150×*g* for 10 min at room temperature. The plasma was then collected and stored at −80°C until subsequent analysis.

2.7. Analysis of plasma by LC-MS/MS-based untargeted metabolomics

Metabolite extraction was conducted by adding 1 mL ice-cold acetonitrile to 100 μL of mouse plasma. Samples were vortexed and placed at −20°C for 45 min to allow proteins to precipitate. After centrifugation at 18,000×*g*, 4°C for 15 min supernatants were transferred to new Eppendorf tubes and samples were evaporated to dryness using a SpeedVac (Eppendorf, model 5301). Dried extracts were kept at −80°C until further analysis. On the day of analysis samples were reconstituted in 100 μL of a 1% methanol solution in water, vortexed and then sonicated for 5 min. After centrifugation at 18,000×*g*, 4°C for 15 min supernatants were transferred to micro-vial inserts. A fixed volume was aliquoted per sample to build a quality control (QC) sample, which was injected periodically across the metabolomics run.

Metabolite extracts were measured in a liquid chromatography tandem mass spectrometry (LC-MS/MS) system, using an in-house metabolite library (Ciurli et al., 2024), according to previously described methods (Kloosterman et al., 2024). Briefly, 10 μL of the samples were injected in a Shimadzu Nexera X2 (Shimadzu, The Netherlands). The mobile phases i.e. water (eluent A) and methanol (eluent B), both with 0.1% formic acid, were pumped at 0.4 mL/min flow rate with the following composition: 0% B at 0 min, 0% B at 1.5 min, 97% B at 9.9 min, 97% B at 12.9 min, 0% B at 13.0 min and 0% B at 13.8 min. The column used was a Synergi Hydro-RP, 2.5 μm, 100 × 2 mm with a Phenomenex SecurityGuard Ultra C8, 2.7 μm, 5 × 2.1 mm guard column cartridge, kept at 40 °C in the column oven. The MS was a Sciex TripleTOF 6600 (AB Sciex Netherlands B.V., The Netherlands) operated in positive and negative ESI mode. An information dependent acquisition (IDA) method was used to identify the different metabolites. Further details on the MS and MS/MS parameters have been published previously (Kloosterman et al., 2024). MS-DIAL (v5.1), was used to align the data and annotate the different metabolites matching accurate mass, retention time and, in most cases, the MS/MS fragmentation pattern against the authentic chemical standards (our in-house metabolite database). Metabolites with the peak area's RSD below 30% in the QC samples and with sample-to-blank ratio above 5 for at least 80% of the samples within the experimental groups were considered for further data analysis. Peak areas were first adjusted for possible trends using QC-based LOESS correction, then areas were normalized to total area for the identified metabolites per sample.

2.8. Analysis of plasma by LC-MS/MS-based untargeted lipidomics

Lipid extraction was conducted by adding 600 μL methyl *tert*-butyl ether (MTBE) and 150 μL methanol to 50 μL of mouse plasma. Samples were vortexed and centrifuged at 18,000×*g*, 20°C for 5 min. Supernatants to new Eppendorf tubes and the extraction was repeated with 300 μL MTBE and 100 μL methanol. After another round of centrifugation, supernatants were finally combined and 300 μL water was further added. Samples were centrifuged at 18,000×*g*, 20°C for 5 min to allow for the two immiscible layers to form. 650 μL from the lipid layer (upper phase) were taken and were evaporated using a gentle nitrogen flow. Dried extracts were kept at −80°C until further analysis. On the day of

analysis samples were reconstituted in 50 μL of 2-propanol, vortexed, sonicated for 5 min, then 50 μL of water was added and samples were further vortexed and sonicated for another 5 min. Samples were transferred to micro-vial inserts. A fixed volume was aliquoted per sample to build a quality control (QC) sample, which was injected periodically across the lipidomics run.

Lipid extracts were measured in the same LC-MS/MS system from the untargeted metabolomics analysis but using different mobile phases, gradient, chromatographic column and MS and MS/MS parameters, as described in detail previously (Singh et al., 2024). Briefly, mobile phases were water:acetonitrile 80:20 (eluent A) and water:2-propanol: acetonitrile 1:90:9 (eluent B), both containing 5 mM ammonium formate and 0.05% formic acid. The applied gradient, with a column flow of 0.3 mL/min, was as follows: 0 min 40% B, 10 min 100% B, 12 min 100% B. A C18 Phenomenex Kinetex, 2.7 μm, 50 × 2.1 mm column with a C8 Phenomenex SecurityGuard Ultra, 2.7 μm, 5 × 2.1 mm pre-column were used. The MS operated in positive and negative ESI mode using an IDA method to identify the different lipids. Full MS and MS/MS parameter settings are provided by Singh et al. (2024). MS-DIAL (v5.1) with the associated standard lipid library was used to align the data and annotate the different lipids matching accurate mass and MS/MS fragmentation pattern. Lipids with the peak area's RSD below 30% in the QC samples and with sample-to-blank ratio above 5 for at least 80% of the samples within the experimental groups were considered for further data analysis. Peak areas were first adjusted for possible trends using QC-based LOESS correction, then areas were normalized to total area for the identified lipids per sample.

2.9. Echocardiography assessment

Eight weeks after the final injection, transthoracic echocardiography was performed. Mice were anesthetized with 2% isoflurane, depilated, and imaged in a supine position with the Vevo 3100 high-frequency ultrasound system equipped with a 40-MHz MX550D transducer (FUJIFILM VisualSonics), as previously described (Qiao et al., 2020; Bankhead et al., 2017). Heart rate (400–600 bpm), respiratory rate (80–120 breaths/min) and temperature (37°C) were continuously monitored. B-mode and M-mode echocardiographic images were obtained in parasternal long-axis (PLAX) and short-axis (SAX) views at the midpapillary muscle level. Four-dimensional echocardiography was acquired at 0.3 mm using a 0.3 mm step size enabling reconstruction of left ventricular volumes and systolic function synchronized to cardiac and respiratory cycles.

Left ventricular diastolic function was evaluated from two-dimensional B-mode tracings in the apical four-chamber view at the level of the atrioventricular valves. Pulsed-wave Doppler at the tips of the mitral valve was used to measure early filling velocity (MV E), atrial wave (MV A) could not be quantified due to fusion of the waves at high heart rates. Tissue Doppler imaging at the septal mitral annulus was performed to quantify the S wave and early diastolic velocity (E′). From these recordings, the MV E/E′ ratio, isovolumetric relaxation time (IVRT), and deceleration time (DT) were derived. Global longitudinal strain was conducted in parasternal long-axis view using B-mode images. Analyses were performed in VevoLAB (FUJIFILM VisualSonics, version 5.9.0) including the VevoStrain 2.0 module. Left ventricular volumes were normalized to tibia length. Recordings were reviewed by two blinded observers, with disagreements resolved by a third consensus. Artifacts preventing reliable assessment were excluded upon agreement.

Following echocardiography, animals remained under anaesthesia and were euthanized by intraperitoneal injection of pentobarbital (800 mg/kg Euthasol, AST Farma, The Netherlands); blood was collected by cardiac puncture (described in section on blood collection) and organs were perfused with saline and harvested.

2.10. Cardiac histology

Perfused hearts were collected, and the apex was transversely excised with a microblade and dissected from the remaining left and right ventricular tissue. The excised apex tissue was fixed overnight in 4% paraformaldehyde, transferred to 70% ethanol, dehydrated, and paraffin embedded. Sections (4 μm) were stained with haematoxylin and eosin (H&E; Histocore, Leica) and Masson's trichrome (Dako Artisan) using standard protocols. Images were acquired with a slide scanner (VS200, Olympus). Cardiomyocyte size was quantified on H&E images and corresponds to the mean cross-sectional area of at least 50 left-ventricular cardiomyocytes. Ventricular fibrosis was quantified on Masson's trichrome sections by pixel classification in QuPath (V0.6.0) (Bankhead et al., 2017) and expressed as percentage of total myocardial area.

2.11. RNA isolation, cDNA synthesis, and qRT-PCR

Snap-frozen left ventricular samples were homogenized in TriPure Isolation Reagent (Roche Diagnostics) using a bead-beater, and RNA was quantified with Qubit 4 Fluorometer (Invitrogen). cDNA was synthesized with the iScript cDNA Synthesis Kit (Quatetect) according to the manufacturer's protocol. Relative gene expression was analysed by quantitative PCR with SYBR Green (Bio-Rad) on a CFX384 Real-Time PCR Detection System (Bio-Rad) using the following primers: RPS18 FW: CGCCGCTAGAGGTGAAATTCT, RV: CGAACCTCCGACTTTCGTTCT; NPPA FW: ATTGACAGGATTGGAGCCCAGAGT, RV: TGACACACCACAAGGGCTTAGGAT; NPPB FW: GTTTGGGCTGTAACGCACTGA, RV: GAAAGAGACCCAGGCAGAGTCA. Reactions were run in duplicate (95°C for 5 min; 40 cycles of 95°C for 30 s, 60°C for 30 s, 70°C for 30 s) followed by melting curve analysis. Expression levels of the natriuretic peptide A gene (*Nppa*) and natriuretic peptide B gene (*Nppb*) were normalized to the reference gene encoding for the ribosomal protein S18 (*Rps18*), and relative fold change was calculated with the 2ˆ−8ΔΔCt method.

2.12. Plasma cytokine multiplex analysis

Plasma cytokine concentrations were determined using the Olink® Target 48 Mouse Cytokine panel (Olink Proteomics AB, Uppsala, Sweden) according to the manufacturer's instructions. This assay is based on the Proximity Extension Assay (PEA) technology, in which pairs of oligonucleotide-labelled antibodies bind to their respective target proteins (Assarsson et al., 2014). Upon dual binding, a proximity-dependent DNA polymerization event generates a reporter sequence that is subsequently amplified and quantified by real-time PCR. Internal and external controls are incorporated at each assay step to monitor technical performance and enable normalization across samples and plates. Quality control was performed using Olink NPX Signature software, which excluded 7 of the 78 samples that did not meet internal QC criteria. The assay output is expressed as Normalized Protein Expression (NPX) on a log2 scale, where higher NPX values reflect higher relative protein abundance.

2.13. Microglia analysis

2.13.1. Brain perfusion and tissue collection

A subsection of male mice treated at ZT2 or ZT14 were sacrificed 24 h after the final injection to evaluate acute microglial effects or three weeks later to evaluate long-term effects. Mice were anesthetized with isoflurane and euthanized by intraperitoneal overdose of pentobarbital (800 mg/kg Euthasol, AST Farma, The Netherlands) while maintained under isoflurane until death. Mice were then transcardially perfused with cold saline (0.9% NaCl in ultrapure H_2O), followed by ice-cold 4% PFA. Brains were post-fixed in 4% PFA at 4°C for 24 h and subsequently transferred to 1% PFA at 4°C for long-term storage. Prior to tissue

slicing, brains were transferred to 30% sucrose at 4°C until saturated. Brain tissues were sliced into 35 μm coronal-sections using a cryostat (Cryostat Crypstar NX70, Thermo scientific), and suprachiasmatic nucleus (SCN) sections were selected from Bregma −0.43 mm to Bregma −0.52 mm. Sections were collected in cryoprotectant solution (300 g sucrose dissolved in 400 mL, added 0.5 g sodium azide, 300 mL glycerol, 300 mL ethyl glycol) and stored at −20°C until further use.

2.13.2. Immunofluorescence of brain slices

Free-floating sections were washed 3x for 5 min each with 1× TBS. Slices were blocked for 30 min in 1× TBS containing 1% normal donkey serum (NDS; 1:100). Primary antibodies: rabbit anti-IBA1 (1:400, #234013, SYSY), rat anti-CD68 (1:100, #53444, Abcam) were diluted in SUMI buffer (gelatine 625 mg, Triton X-100, 1.25 mL, 250 mL 1× TBS all dissolved at 45°C, pH 7.6) for overnight incubation at 4°C. The following day, sections were washed 3× for 5 min in 1× TBS, then incubated for 1 h with biotinylated anti-rat IgG (1:400, #BA9400, Vector Laboratories) at room temperature. After three additional washes in 1× TBS, sections were incubated for 1 h at room temperature with donkey anti-rabbit AF488 (1:400, #A21206, Invitrogen), streptavidin Alexa Fluor 546 (1:800, #S11225, Invitrogen), both diluted in SUMI buffer. After the incubation, slices were washed 3× for 5 min with 1× TBS. The sections were then incubated in NeuroTrace (1:400, #N21483, Thermo Fisher Scientific) for 20–30 min at room temperature, followed by 3× wash. Nuclear counterstaining was performed using DAPI (1:500, #62247, Thermo Fisher) for 10–15 min and then 3× washed with 1x TBS. Finally, sections were mounted on Superfrost Plus slides (Thermo Fisher Scientific) and cover slipped using antifade mounting medium (#H-1700, Vector Laboratories).

Quantification of imaging data was conducted in a blinded manner, where IBA1-immunoreactive (IBA1-ir) cell numbers and ramifications were manually counted, and the volume of CD68-immunoreactive (CD68-ir) and IBA1-ir were quantified by Imaris software with 3D reconstruction (Bitplane AG, Zurich, Switzerland). Microglial soma, whole-cell and skeletonized parameters were quantified using script AutoMorFi as previously described (Bouadi et al., 2024).

2.14. Statistics

Statistical analyses were performed in R (version 4.4.0) (R Core Team, 2024) and GraphPad Prism (version 9.5.1). Linear mixed-effects models (emmeans (Lenth, 2025), lme4 (Bates et al., 2015) and lmerTest (Kuznetsova et al., 2017) with mouse-specific random intercepts were used to test ZT group × time (days) effects for running wheel activity, cage activity, body weight, and ZT group × hour interactions for daily activity patterns. Post hoc pairwise comparisons were corrected using the Dunnett's procedure. One-way ANOVA with Tukey's post hoc test was used for grip strength, circadian parameters, metabolites, lipids, and normally distributed Olink proteins, while non-normally distributed Olink proteins were analysed by Kruskal–Wallis with Dunn's test and Benjamini–Hochberg correction. Echocardiographic data were analysed by Kruskal–Wallis with Dunn's test or unpaired *t*-test, and SCN imaging data by two-way ANOVA.

Metabolite and lipid data were log-transformed, and z-score were calculated by subtracting the group mean and dividing by the group standard deviation. Patterns were explored by principal component analysis, and outliers were defined with Hotelling's T2 ellipse analysis. Subsequently, a one-way ANOVA with ZT group as the independent variable was conducted to assess the effect of the time of treatment, and results with non-adjusted p-values < 0.05 were visualised in heatmaps and used for subsequent analysis. Pathway analysis was conducted in MetaboAnalyst (Pang et al., 2024), using the provided *mus musculus* KEGG pathway library as a reference metabolome. Olink proteomic data were additionally explored by principal component analysis and tested for differential abundance using limma (version 3.62.2). Results were visualized with Enhanced Volcano (version 1.24.0) and Complex Heatmap (version 2.16.0), with proteins considered differentially expressed at FDR < 0.05 and absolute $\log^2$ fold change ≥ 0.05. Significance was defined as $p < 0.05$ (*$p < 0.05$; ** $p < 0.01$; ***$p < 0.001$). Boxplots indicate the interquartile range (IQR) with median, and whiskers denote minimum (−1.5 * IQR) and maximum values (+ 1.5 * IQR). Bar graphs present means + SEM.

3. Results

3.1. Time of treatment affects severity of doxorubicin-induced fatigue in mice

To evaluate the effect of the time of treatment on the development and underlying pathways of doxorubicin-induced fatigue, we treated four groups of mice with doxorubicin at different times of day (ZT2, ZT8, ZT14 and ZT20). All doxorubicin-treated animals showed reduced running wheel activity and home-cage activity compared to pre-treatment activity levels (Fig. 1a-c). Interestingly, mice treated at ZT14 showed a more severe fatigue phenotype, which persisted up to the end of the experiment, six weeks post-treatment. Linear mixed-effect models revealed a significant interaction between post-treatment days and injection time for running wheel activity ($p = 0.011$), and cage activity ($p < 0.001$). Post hoc tests for running wheel activity revealed differences between ZT14 and ZT8 at day 39–41 and day 43 (Supplementary Table 1). For cage activity, post hoc testing revealed significant differences between mice treated at ZT14 and one or more groups on days 6, 15, 23–28, 30, 33, 35–43 ($p < 0.05$) (Supplementary Table 1). To further investigate these differences, we assessed the running wheel activity profiles of the ZT groups at baseline, and post-treatment in LD and DD conditions. Prior to treatment, no significant interaction effects were detected between groups over 24 h ($p = 0.521$) (Fig. 1d). After treatment, a significant interaction effect between time of day and injection time was detected in LD ($p < 0.001$) (Fig. 1e) and DD ($p = 0.004$) (Fig. 1f). Post hoc analysis shows a significant difference ($p < 0.05$) between various groups in the active period (Supplementary Table 1). Analysis of post-treatment cumulative running distance across the mice revealed a significant interaction between injection time and day ($p < 0.001$) (Fig. 1g), showing that mice treated at ZT14 ran significantly less from day 21 onwards ($p < 0.05$, Supplementary Table 1). Furthermore, a significant effect of injection time on body weight was found ($p < 0.001$) and the estimated marginal means showed reduced weight at day 9 for mice treated at ZT14 (vs ZT2, $p = 0.003$ and vs ZT20, $p = 0.005$) (Supplementary Fig. 1a). After treatment, mice treated at ZT14 recovered swiftly in weight to levels similar to the other groups. At sacrifice mice treated at ZT2 showed smallest relative weight gain (compared to those at ZT14, $p = 0.046$ and ZT20, $p = 0.007$). No effect of time of treatment was observed for grip strength one and three weeks after completion of treatment (Supplementary Fig. 1b, c). This indicates that fatigue as measured by voluntary wheel activity, is not merely a secondary consequence of general physical decline, but rather a time-specific result of treatment at ZT14.

As we have previously shown that doxorubicin can disturb the circadian system (Wang et al., 2022), we assessed whether such disruption depended on the time of treatment by evaluating multiple aspects of circadian rhythmicity. This included the assessment of rhythm strength, intradaily variability (IV), and interdaily stability (IS), capturing the amplitude, fragmentation, and day-to-day stability of the rest–activity rhythm. Additionally, we analysed phase angle of entrainment, activity duration (α), day/night activity ratio, capturing circadian timing and activity distribution across light–dark cycle at baseline and post-treatment. No significant differences were observed post-treatment between doxorubicin-treated groups in LD for circadian rhythm strength ($F(3, 25) = 1.89$; $p = 0.16$), IV ($F(3, 25) = 2.44$; $p = 0.09$), IS ($F(3, 25) = 1.76$; $p = 0.18$) (Supplementary Fig. 2a-c), phase angle of entrainment ($F(3,26) = 0.43$, $p = 0.74$), α duration ($F(3,26) = 0.35$, $p = 0.79$), day/night activity ratio ($F(3,26) = 0.77$, $p = 0.52$)

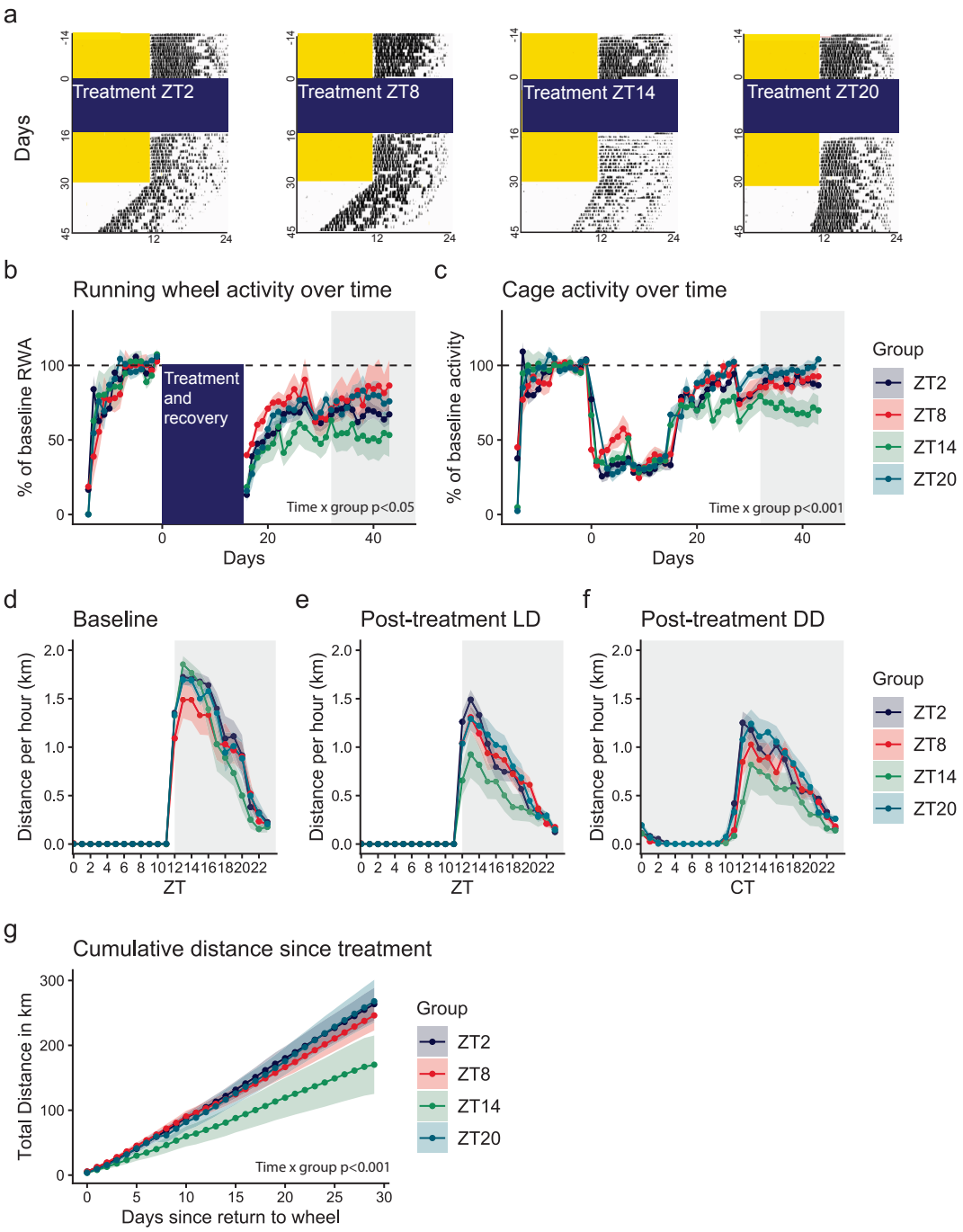

Fig. 1. Doxorubicin treatment at ZT14 induces greater reduction of voluntary activity. (a) Representative actograms from each treatment group illustrate wheel rotations across the study. (b) Voluntary running wheel activity during the experiment relative to baseline. (c) Cage activity measured with passive infrared detection relative to baseline. Average hourly running distance is shown for (d) baseline conditions, during (e) post-treatment light–dark cycles and during (f) constant darkness. (g) Cumulative running distance after treatment. Group sizes were ZT8 (n = 7) and all other groups (n = 8); female mice. Statistical testing using a linear mixed-effects model with time, ZT group, and time x group as (categorial) fixed effects and mouse as random effect. Shaded areas represent standard error of the mean. ZT: zeitgeber time; CT: circadian time; LD: 12:12 light–dark cycle; DD: constant darkness.

(Supplementary Fig. 3). Similarly, no significant effect was observed in DD for circadian rhythm strength ($F(3, 28) = 1.80$; $p = 0.17$) nor for IV ($F(3, 26) = 0.89$; $p = 0.46$) (Supplementary Fig. 2d-e). For free running period (τ) an effect was seen for group ($H(3) = 10.2$, $p = 0.017$), with a significant difference between ZT2 and ZT8 treated animals ($p = 0.02$) (Supplementary Fig. 2f). Altogether, these results indicate that time-of-treatment primarily impacts the magnitude of active-phase running wheel activity, rather than affecting circadian period, entrainment or rest-activity rhythms.

3.2. *Doxorubicin-induced fatigue is independent of doxorubicin-induced cardiotoxicity*

To further explore factors influencing voluntary wheel activity, we examined whether the most severe fatigue phenotype induced by treatment at ZT14 coincided with the development of cardiotoxicity. Doxorubicin-induced cardiotoxicity is typically characterized by histological alterations, including cardiomyocyte atrophy and loss of myofibrils, by impairment of both systolic and diastolic function, and by the

upregulation of molecular markers of cardiac damage, although the exact manifestations vary across murine models (Bayer et al., 2024; Lei et al., 2023).

In our experiment, doxorubicin-treated mice displayed a significant reduction in left ventricular ejection fraction (LVEF) (53.9 ± 7.1% vs 60.8 ± 7.8%, $p = 0.023$) and global longitudinal strain (GLS) (−17.6 ± 1.6 cm/s vs −19.3 ± 1.8 cm/s, $p = 0.022$) when compared to vehicle-treated controls regardless of the time of treatment (Fig. 2a). At the molecular level, the expression of heart-failure associated genes natriuretic peptide B (*Nppb*) and natriuretic peptide A (*Nppa*) was significantly elevated in doxorubicin-treated hearts compared with vehicle-treated controls ($p = 0.007$ and $p < 0.0001$, respectively) (Fig. 2b).

When considering the time of treatment, mice treated at ZT8 showed cardiomyocyte atrophy 10 weeks after the first injection. This was reflected by a smaller mean cross-sectional cardiomyocyte area compared with ZT14, ZT20, but not with ZT2 (Fig. 2c). This contrasted with other histological observations indicating cardiac remodelling, such as the extent of myocardial fibrosis, which did not differ across injection times (Fig. 2d). Moreover, no significant differences in left ventricular systolic- or diastolic functions were observed between the four ZT groups, including LVEF, end-diastolic volume (LVEDV), and the GLS (Fig. 2e), nor in diastolic parameters: S wave, mitral inflow velocity to early diastolic tissue velocity ration (MVE/E'), isovolumetric relaxation time (IVRT), and deceleration time (DT) (Supplementary Fig. 4a). In line with the functional data, no significant differences were observed in *Nppb* and *Nppa* expression levels across ZT groups, suggesting that the molecular response in left ventricular tissue to doxorubicin was not affected by the time of doxorubicin treatment (Supplementary Fig. 4b).

3.3. Systemic inflammation after doxorubicin is attenuated when treated at ZT8 and ZT14

While prolonged low-grade systemic inflammation has been previously associated with cancer and chemotherapy-induced chronic fatigue in patients (Bower and Lamkin, 2013), there is still limited understanding of the time-dependent inflammatory response to doxorubicin as a potential factor related to chemotherapy-induced fatigue. Therefore, plasma concentrations of 43 cytokines were analysed at one and three weeks following the last injection with doxorubicin. Principal component analysis of these data revealed overlap between ZT groups, with no clear separation along PC1 (24.8%) nor PC2 (10.7%) (Fig. 3a). However, a separation of the week 1 and week 3 post-injection samples was visible in PC1, suggesting that while time of doxorubicin administration did not drive global expression patterns, differences in the inflammatory response between week 1 and 3 contributed to subtle alterations in the cytokine profile. In total, 7 out of the 20 significant cytokines passed the cut-off filter of p-value of 0.05 and log FC of 0.5 after doxorubicin administration (Supplementary Fig. 5a). At week 1, cytokine levels were largely overlapping across groups, although post hoc analysis revealed lower levels of the pro-inflammatory cytokines TNF-α and CXCL9 in mice treated at ZT14 (Fig. 3b). After three weeks, time-dependent differences in cytokine levels became more evident, with more cytokines showing significant differences between injection times. Mice treated at ZT2 and ZT8 displayed higher cytokine levels, whereas ZT14 and ZT20 were characterized by lower levels of plasma cytokines, specifically CXCL9, TNF-α, CCL5, CSF2 at ZT14, and CCL22 and CCL5 at ZT20 (Supplementary Fig. 5).

3.4. Metabolite and lipidomic profiles are affected by the time of doxorubicin administration

To explore the impact of the time of treatment on metabolite and lipid profiles, both untargeted metabolomic and lipidomic analyses were performed in plasma samples from 28 doxorubicin-treated mice. In total, 127 metabolites were identified in these samples. Principal component analysis with a Hotelling's T2 ellipse identified four outliers which were

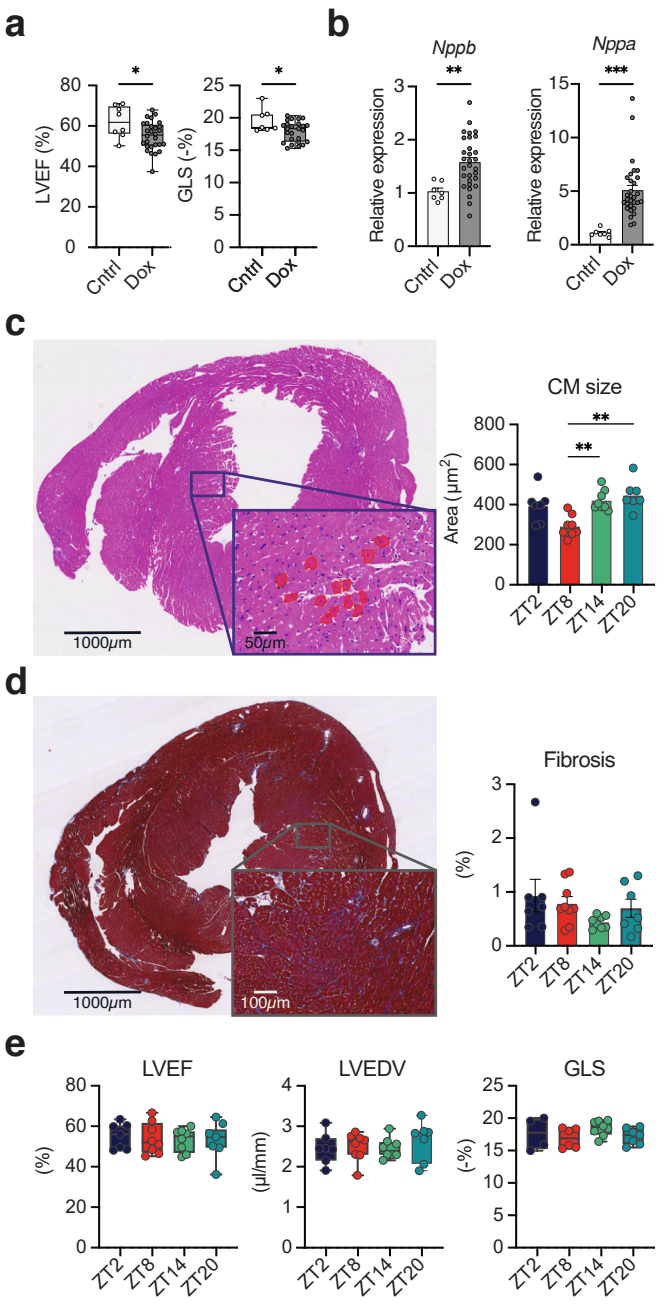

Fig. 2. Chronic doxorubicin exposure induces mild cardiotoxicity in absence of a chronopharmacological effect in mice. (a) Left ventricular ejection fraction (LVEF) and global longitudinal strain (GLS) assessment for control (n = 8) vs doxorubicin-treated female mice (n = 30). (b) Relative quantification of mRNA levels of *Nppb* (brain natriuretic peptide) and *Nppa* (atrial natriuretic peptide) in murine hearts for control (n = 8) vs doxorubicin-treated mice (n = 30). (c) Representative image of H&E staining and quantification of cardiomyocyte size per ZT-group (ZT2, ZT8, ZT14, ZT20; n = 7, 8, 8, 7 mice, respectively, per group) in myocardial sections. (d) Representative image of MT staining and quantification of collagen deposition per ZT-group (ZT2, ZT8, ZT14, ZT20; n = 7, 8, 8, 7 mice per group) in myocardial sections. (e) Echocardiographic assessment of systolic function; left ventricular ejection fraction (LVEF), left ventricular end-diastolic volume (LVEDV (ZT2, ZT8, ZT14, ZT20; n = 7, 8, 8, 7 mice, respectively, per group); and global longitudinal strain (GLS) (ZT2, ZT8, ZT14, ZT20; n = 4, 6, 8, 7 mice, respectively, per group). Statistical analysis was performed using a two-tailed unpaired *t*-test or one-way ANOVA followed by Tukey's HSD for multiple comparisons.

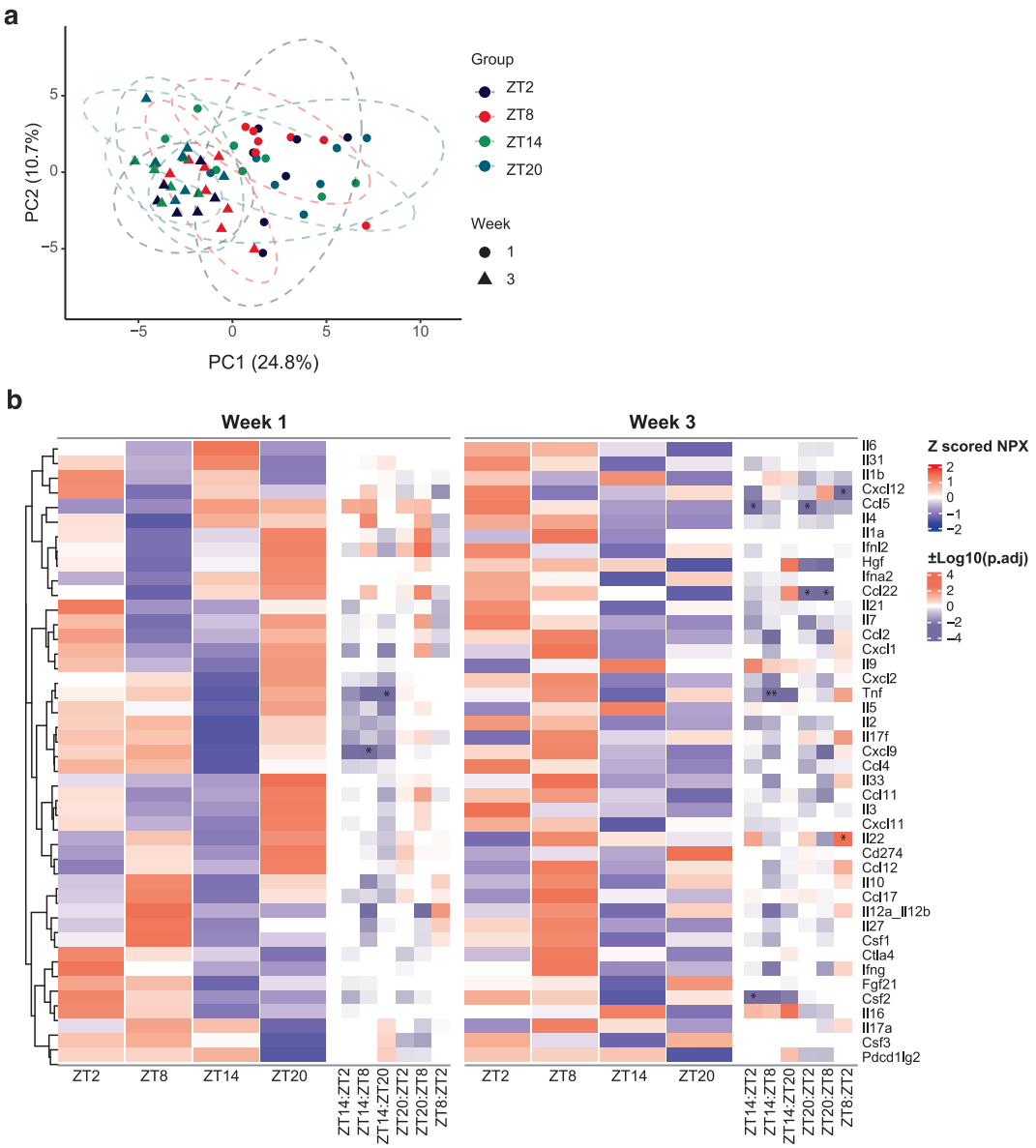

Fig. 3. Time of treatment differences in serum cytokine expression. (a) Principal component analysis of Olink inflammatory cytokine panel data in mouse plasma at week 1 (circle) and 3 (triangle), stratified by ZT groups. Each point represents an individual sample, and ellipses represent 95% confidence intervals. (b) Heatmap of 43 inflammatory cytokines across ZT groups at week 1 (ZT2, ZT8, ZT14, ZT20; n = 6, 7, 8, 7 samples, respectively, per group, female mice) and week 3 (ZT2, ZT8, ZT14, ZT20; n = 6, 8, 8, 7, respectively, samples per group, female mice). Left panels show Z-scored NPX values per group. Right panels display pairwise group comparisons as signed log10 (adjusted p-values), where the sign corresponds to the direction of the estimated difference in mean NPX between groups The magnitude reflects the level of statistical significance (e.g. |1| = p.adj 0.1; |2| = p.adj 0.01). Positive values (orange) denoting higher protein abundance in the first-named group and negative values (purple) denoting lower abundance. Asterisks indicate statistical significance (*$p < 0.05$, **$p < 0.01$). Normally distributed cytokines were analysed by two-way ANOVA with Tukey's HSD; non-normally distributed cytokines by Kruskal–Wallis with Dunn's post hoc test and Benjamini–Hochberg correction.

excluded from further analysis (Supplementary Fig. S6a). One-way ANOVA with the time of treatment as the independent variable subsequently identified 31 metabolites significantly affected in plasma of mice treated at different times (Fig. 4a). Subsequent pathway enrichment analysis identified pathways related to aromatic amino acid biosynthesis and metabolism (Supplementary Table 2). In particular, the phenylalanine, tyrosine, and tryptophan biosynthesis pathway was identified (3 of 4 metabolites matched; $p < 0.001$, FDR < 0.001; impact = 1.0). In addition, the phenylalanine metabolism was significantly affected (3 of 10 metabolites matched; $p < 0.001$; FDR = 0.006; impact = 0.62). Interestingly, the metabolites associated with these pathways (phenylpyruvate; tryptophan, phenylalanine, and tyrosine), were increased in mice treated at ZT14 (Fig. 4a). Overall, these changes highlight deviations in core amino acid pathways.

Subsequently, using untargeted lipidomic analysis on the same plasma samples 591 lipids across 39 lipid (sub)classes were detected. Principal component analysis with a Hotelling's T2 ellipse identified two samples as outliers, which were excluded from further analysis (Supplementary Fig. 6b). One-way ANOVA with the time of treatment as the independent factor identified 69 lipids significantly affected by the time of treatment, spread across 14 different lipid (sub)classes (Fig. 4b). There were some distinct patterns associated with treatment at ZT14 such as an increase of triacylglycerols (TGs) and an increased pool of saturated free fatty acids (FAs) accompanied by a decrease in glycerophospholipids such as phosphatidylcholines (PCs), lysophosphatidylethanolamines (LPEs) and ether-linked phosphatidylethanolamines (PE-

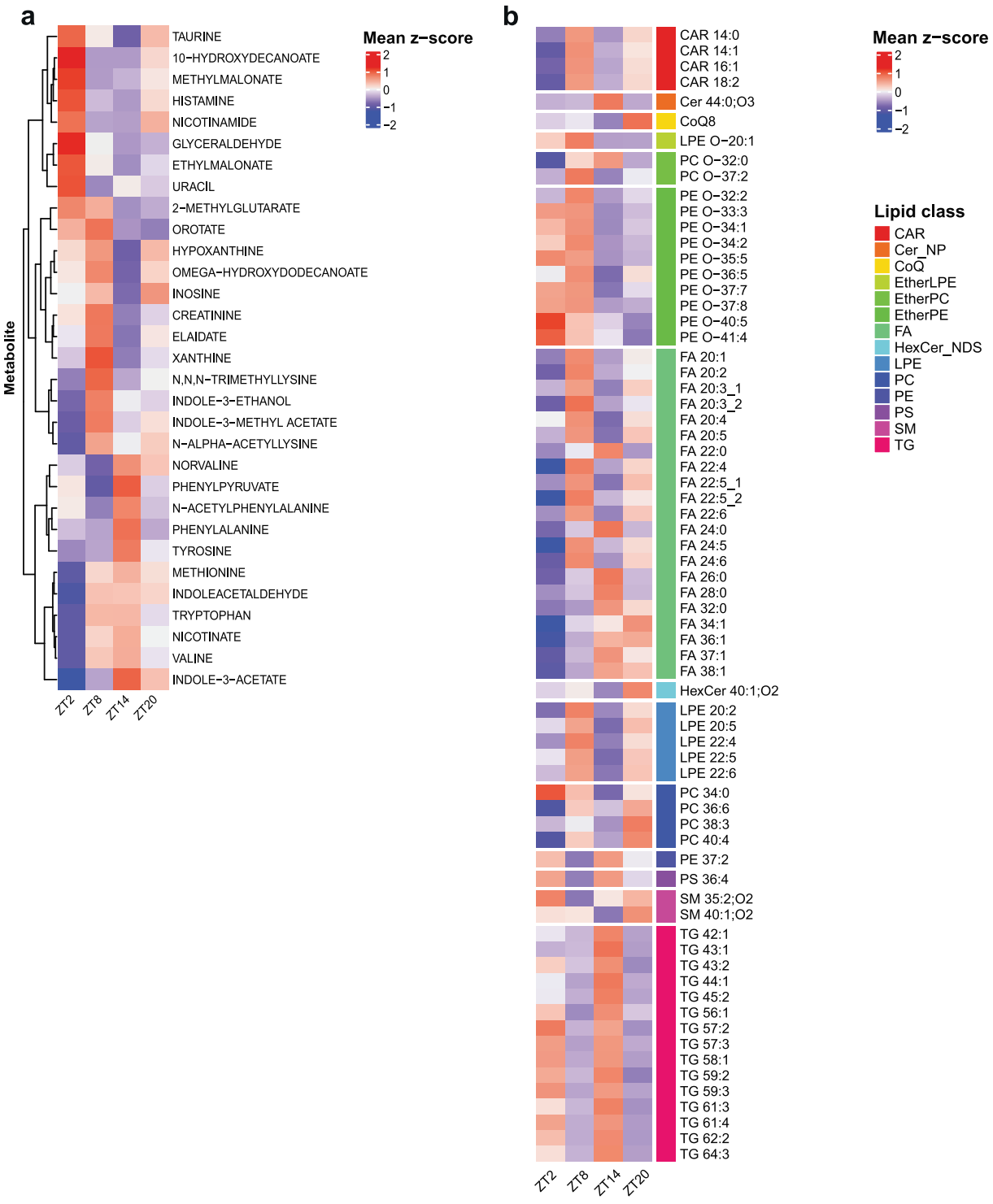

Fig. 4. Metabolites and lipid class profiles are altered by time of treatment. (a) Heatmap of 31 metabolites significantly affected by the time of treatment at sacrifice (one-way ANOVA), showing normalised abundance across ZT groups. Clustering by the time of treatment indicates that chemotherapy induces ZT-dependent metabolomic signatures (ZT2, ZT8, ZT14, ZT20; n = 5, 7, 8, 6 female mice, respectively, per group). (b) Heatmap of lipid classes significantly affected by ZT group (one-way ANOVA), showing normalised abundance across ZT groups. Clustering by the time of treatment indicates that chemotherapy alters lipid class composition in a time-dependent manner (ZT2, ZT8, ZT14, ZT20; n = 3, 8, 8, 7 female mice, respectively, per group). CAR, acylcarnitine; Cer_NP, non-hydroxy-fatty acid phytosphingosine ceramide; CoQ, coenzyme Q; EtherLPE, ether-linked lysophosphatidylethanolamine; EtherPC, ether-linked phosphatidylcholine; EtherPE, ether-linked phosphatidylethanolamine; FA, fatty acids; HexCer_NDS, hexosylceramides (with N-deoxysphingoid base); LPE, lysophosphatidylethanolamine; PC, phosphatidylcholine; PE, phosphatidylethanolamine; PS, phosphatidylserine; SM, sphingomyelin; TG, triglyceride. Different isomers for fatty acids indicated with_1 and_2.

Os). Together, both metabolomic and lipidomic findings point to time-of-treatment dependent remodelling in both the amino acid-related metabolism and in membrane-associated lipid pathways.

3.5. Mice treated at ZT14 show an altered microglial state in the SCN

Given the persistence of fatigue following treatment and the previously established association between disruption of the SCN and doxorubicin treatment, we next examined whether doxorubicin treatment influenced microglial activation within the SCN and whether this is depending on the time of treatment (Fig. 5a). As treatment at ZT14 induced the most severe phenotype, whereas no differences were observed among ZT2, ZT8 and ZT20, subsequent analyses, focused on mice treated at ZT2 and ZT14. These timepoints represent opposite phases of the light–dark cycle (early rest versus early active period, respectively). Outcomes were evaluated both 24 h and three weeks after the final doxorubicin injection.

24 h after completion of doxorubicin treatment, no significant differences were observed between ZT2 and ZT14 in terms of Iba1 + microglial cell numbers ($p = 0.251$) and primary ramifications ($p = 0.70$) (Fig. 5b,c). CD68 size per microglia was increased in ZT14 treated animals, albeit not significantly ($p = 0.06$) (Fig. 5d). At 3 weeks post-treatment, no differences were observed in Iba1 cell numbers ($p = 0.784$) or size ($p = 0.442$) (Fig. 5e,f). Primary ramifications were lower in the mice treated at ZT14 than those treated at ZT2, though not significant ($p = 0.070$) (Fig. 5g). In contrast, higher CD68 + volume normalized to Iba1 + microglial volume was observed (Fig. 5h) in ZT14 compared to ZT2 ($p = 0.049$, as well as larger CD68 size per microglia ($p = 0.046$), Fig. 5i).

When examining the overall effects of doxorubicin on microglial

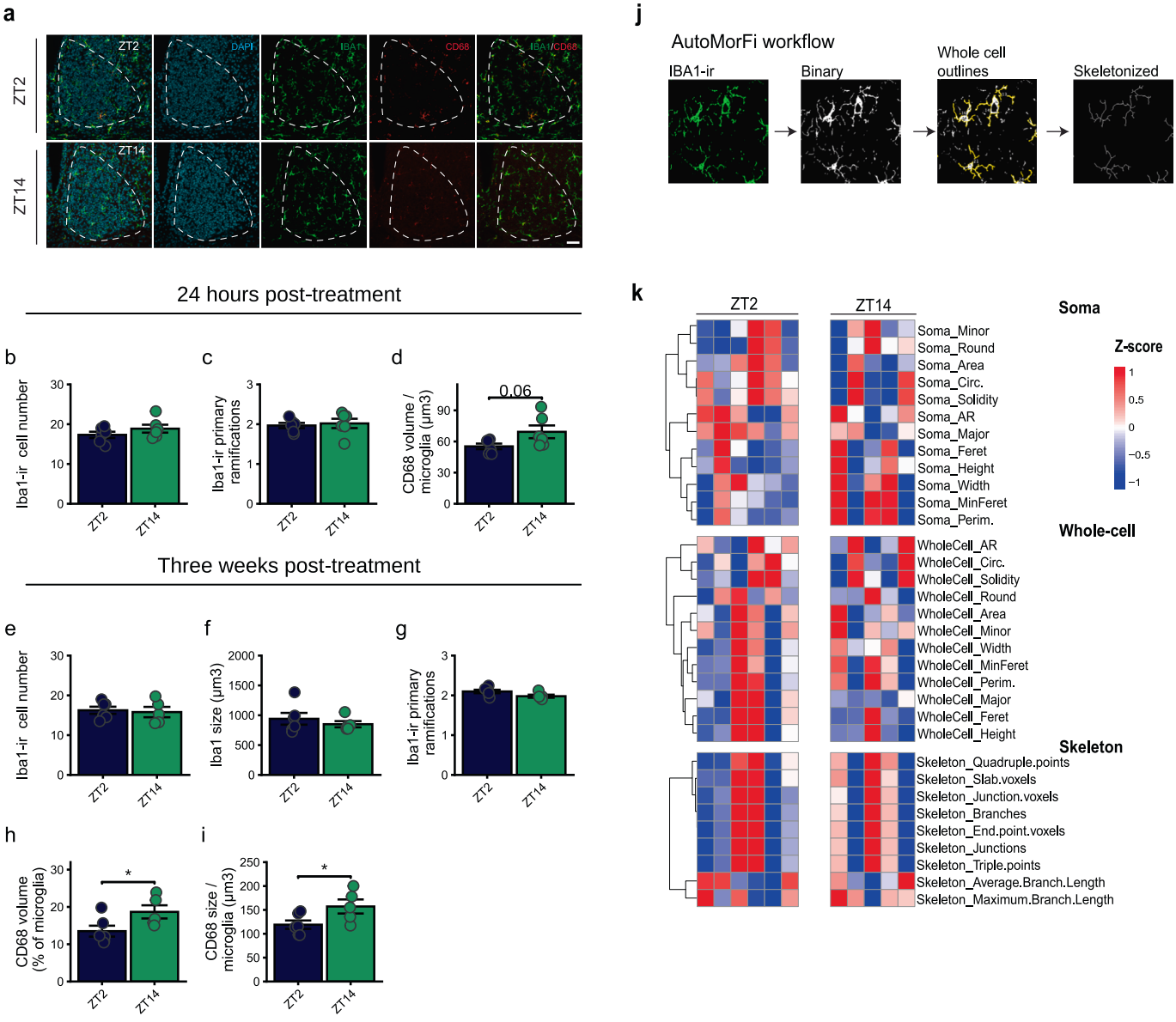

Fig. 5. Microglial morphology and phagocytic phenotype differ between ZT2 and ZT14 treated male mice. (a) Representative images of CD68 expression in Iba1-immunoreactive (Iba1-ir) microglia at ZT2 and ZT14. Analyses 24 h after final injection: (b) mean number of Iba1-positive cells, (c) mean number of primary ramifications per microglia, and (d) mean CD68 size per microglia (μm^3; $n = 6$ per group). Analyses 3 weeks post-treatment: (e) mean number of Iba1-positive cells, (f) mean Iba1 size (μm^3), (g) mean number of primary ramifications per microglia, (h) mean CD68 volume relative to Iba1 volume, and (i) mean CD68 volume per microglia (μm^3) per group ($n = 6$ for ZT2, $n = 5$ for ZT14). Comparisons were performed with t-tests; * represents $p < 0.05$. (j) AutoMorFi analysis workflow and (k) corresponding heatmap summarising differences in microglial morphology features between ZT2 and ZT14 groups. Definition of these features are available in Supplementary Table 3.

activation three weeks after doxorubicin treatment, no significant differences were observed between doxorubicin- and vehicle-treated groups in Iba1 + microglial cell number ($p = 0.588$), cell size ($p = 0.514$), or primary ramifications ($p = 0.343$) (Supplementary Fig. 7a–c). In contrast, CD68 + volume normalised to Iba1 + microglial volume was significantly increased ($p = 0.011$), as was CD68 + volume per microglia ($p = 0.013$) (Supplementary Fig. 7d,e) after doxorubicin treatment compared to vehicle treatment. When the same parameters were analysed according to treatment time, both were significantly higher in animals treated with doxorubicin at ZT14 than in those treated at ZT2 (Fig. 5h,i), indicating that the overall increases were primarily driven by the ZT14 group. Importantly, no significant differences in microglial activation were detected between the vehicle-treated animals in both ZT groups (Supplementary Fig. 7). Together, these observations suggest that microglia in the SCN exhibit an elevated phagocytic state three weeks following doxorubicin treatment, which was more pronounced following administration at ZT14 compared with ZT2.

Subsequent morphological analysis was conducted via AutoMorfi (Fig. 5j). No discernible patterns were observed across soma, whole cell, and cytoskeleton parameters for either group, suggesting that, within the limits of our assay, the time of treatment did not induce a detectable alteration in microglial morphology (Fig. 5k).

4. Discussion

Cancer-related fatigue is a prevalent long-term side effect of cancer therapy, yet its pathophysiological mechanisms remain poorly understood, limiting the development of effective interventions. Our findings highlight the potential of chronopharmacological approaches to mitigate chemotherapy-induced fatigue. We demonstrated that doxorubicin administration at ZT14, corresponding to the early active phase, elicits a more exacerbated fatigue phenotype compared to treatment at other times of day. The dependence of fatigue severity on the time of treatment allowed us to discriminate between the general toxic effects of doxorubicin and the fatigue-inducing mechanisms. At ZT14 we also observed changes in microglial activity, and distinct metabolomic, lipidomic and cytokine signatures indicating their involvement in fatigue. Surprisingly, cardiotoxicity appeared unrelated. Together, these data support the view that fatigue is mechanistically distinct from other general toxicities, and that its impact can be attenuated by consideration of treatment time.

Mice treated at ZT14 showed more doxorubicin-induced fatigue compared to other times of treatment (ZT2, ZT8 and ZT20). This was illustrated by a greater reduction in voluntary wheel running and home-cage activity, persisting at least for six weeks post-treatment. Importantly, this reduction in voluntary activity, did not coincide with a reduction in grip strength or body weight. This indicates that fatigue does not result from general weakness, consistent with earlier reports (Zombeck et al., 2013; Flanigan et al., 2018). Given that cardiotoxicity is a major dose-limiting effect of doxorubicin, we also explored whether the occurrence of fatigue could reflect doxorubicin-induced cardiac dysfunction. In our study, intravenous doxorubicin administration resulted in mild functional impairment, without time of treatment-dependent differences, as reported by others (Kelters et al., 2025). This raises the question whether time-dependent effects may only become detectable in the setting of severe cardiac dysfunction. These discrepancies in extent of cardiotoxicity might relate to methodological differences, such the access to a running wheel, which has shown cardioprotective effects in rodents (Hayward et al., 2012; Wang et al., 2024). Other factors may include lower cumulative anthracycline dosing, route of administration, or differences in rodent species, strain or sex. Overall, our data do not support a role for cardiotoxicity to explain the observed fatigue.

To evaluate systemic inflammation as an underlying mechanism of fatigue we quantified plasma cytokine levels. Three weeks after the final doxorubicin injection, a time-of-treatment-dependent divergence emerged, with lower cytokine levels in ZT14 and ZT20 compared to ZT2 and ZT8, consistent with Borniger et al. (2017). Interestingly, we show that mice treated at ZT14 displayed more fatigue than those treated at ZT20, despite comparable cytokine levels. Chemotherapy-induced inflammation can disrupt peripheral circadian clocks via cytokine-mediated signalling pathways including IL-6, TNF-α, MCP-1 thereby contributing to the development or maintenance of fatigue (Kim et al., 2019; Wood et al., 2006; Mahoney et al., 2013). However, pharmacological inhibition of cytokine signalling, notably IL-6 (Grossberg et al., 2020; Scott et al., 2022) or IL-1 (Grossberg et al., 2018), was insufficient to prevent chemotherapy- or cancer-induced fatigue. Consequently, systemic inflammation appears to act as a modulator, rather than a primary driver.

Metabolomic analysis revealed enrichment of amino-acid metabolism related pathways in mice treated at ZT14, which have previously been associated with fatigue in cancer patients (Chou et al., 2022). These pathways are instrumental in the synthesis of dopamine, noradrenaline, serotonin, and melatonin, neurotransmitters that regulate motivation, alertness, mood, and circadian rhythmicity (Teleanu et al., 2022; Cajochen et al., 2003). As our measurements were performed in plasma, further research is required to determine their availability in the central nervous system. Furthermore, a time-of-treatment effect on the lipidome was observed: animals treated at ZT14 showed higher levels of TGs and saturated FAs and lower levels of glycerophospholipids. This aligns with previous reports where higher lysophosphatidylcholines (LPCs) levels correlate with a less fatigue in colorectal cancer survivors, and lower levels of phosphatidylcholines (PCs) were observed in individuals with chronic fatigue syndrome (van Roekel et al., 2023; Naviaux et al., 2016). Such shifts may reflect membrane lipid remodelling to support energy storage or adaptation to oxidative stress.

Given that neuroinflammation has been implicated in CRF (Sullivan et al., 2022; Loman et al., 2019), we investigated neuroinflammatory responses in the SCN following doxorubicin treatment at ZT2 and ZT14. Microglia, the primary responders to immune challenges, play a crucial role in preserving neuronal homeostasis. Although microglia number and morphology were unaffected, microglia displayed features consistent with an enhanced phagocytic phenotype following doxorubicin treatment with the strongest effect observed in mice treated at ZT14. An increased CD68 expression reflects a more reactive microglial state and may indicate enhanced synaptic pruning or clearance of stressed neuronal material in response to chemotherapy-induced inflammation.

Attenuating microglial activation can reverse negative neurocognitive effects of doxorubicin (Allen et al., 2019), but its role in fatigue specifically has not yet been established. We previously showed that fatigue is a disorder of wakefulness, rather than an enhanced sleep need (Wang et al., 2022), possibly driven by reduced SCN-mediated arousal. Doxorubicin alters the functionality of the SCN output, rendering disrupted rhythmicity surrounding the SCN (Wang et al., 2024). Such disruptions may extend to downstream pathways through the dorsomedial and lateral hypothalamus, regions through which the clock modulates orexin-dependent arousal and locomotion. Indeed, orexin neuronal activity is decreased after cytotoxic chemotherapy, while administration of orexin reversed chemotherapy-induced fatigue (Weymann et al., 2014). As microglia can remodel synaptic connections through phagocytic mechanisms, increased microglial activation may provide a mechanistic link between disruption in the output of the SCN and the development of fatigue. The causality of these SCN neuroimmune changes requires further validation. Future studies should include additional neuroinflammatory readouts, across downstream brain regions to determine whether broader region-specific immune changes contribute to chemotherapy-induced fatigue.

While the use of a non–tumour-bearing model does not capture the complexity of clinical doxorubicin treatment, including tumour-host interactions, combination treatment and supportive co-medications (i.e. glucocorticoids), it allowed us to isolate the direct adverse effects of doxorubicin. This model provided a controlled platform to examine

timing effects and distinguish fatigue-specific mechanisms from general anthracycline toxicity. Doxorubicin treatment during the early active phase, comparable to early morning in humans, exacerbated fatigue and coincided with increased microglial phagocytic state in the SCN, suggesting a time-dependent neuroimmune contribution of this hypothalamic region to the observed fatigue phenotype. It remains to be studied whether these time-of-day variations stem from circadian pharmacokinetics, intrinsic microglial rhythms, or blood–brain barrier permeability, or a combination of these mechanisms. Overall, we propose the timing of anthracycline administration as a promising strategy to mitigate chemotherapy-induced fatigue and provide a rationale for further translational and clinical evaluation of chronomodulated treatment regimens.

Data sharing statement

The authors confirm that the data supporting the findings of this study are available within the article and/or its supplementary materials. Upon reasonable request, additional details are available from the corresponding author.

CRediT authorship contribution statement

Anneke Kastelein: Writing – review & editing, Writing – original draft, Visualization, Software, Project administration, Methodology, Investigation, Formal analysis, Data curation, Conceptualization. **Ilse R. Kelters:** Writing – review & editing, Writing – original draft, Visualization, Software, Methodology, Investigation, Formal analysis, Data curation, Conceptualization. **Amy Chin On:** Writing – review & editing, Investigation, Data curation. **Han Jiao:** Writing – review & editing, Visualization, Formal analysis. **Sonia Martinez Arenas:** Writing – review & editing, Investigation, Formal analysis. **Rico J.E. Derks:** Formal analysis, Writing - review&editing. **Elena Sánchez-López:** Writing – review & editing, Writing – original draft, Methodology, Investigation. **Anke M. Smits:** Investigation, Resources, Writing – review & editing. **Francesco Angeli:** Writing – review & editing, Validation. **Marco Guglielmo:** Writing – review & editing, Resources. **Joost P.G. Sluijter:** Funding acquisition, Resources, writing – review & editing. **Martin Giera:** Writing – review & editing, Resources. **Chun-Xia Yi:** Writing – review & editing, Resources, Methodology. **Jacques Neefjes:** Writing – review & editing, Supervision, Resources, Funding acquisition. **Vasco Sampaio-Pinto:** Writing – review & editing, Supervision. **Laura Kervezee:** Writing – review & editing, Validation, Supervision, Software, Conceptualization. **Linda W. van Laake:** Writing – review & editing, Supervision, Resources, Funding acquisition. **Johanna H. Meijer:** Writing – review & editing, Supervision, Resources, Funding acquisition.

Funding

A.K. is financed by a Spinoza grant from the NWO awarded to J.N (SPI 93-539). V.S.-P. is supported by a Netherlands Heart Institute postdoctoral fellowship. J.P.G.S. is supported by ZonMw Psider-Heart (10250022110004), NWO-TTP HARVEY (2021/TTW/01038252), H2020-EVICARE (725229) of the European Research Council (ERC), and the PLN foundation. V.S.-P. and J.P.G.S. are supported by ERA for Health Cardinnov (RESCUE- 2024/KIC/01627794). I.R.K. and L.W.v.L. are supported by the Dutch Heart Foundation: Dekker Senior Clinical Scientist 2019, grant agreement number 2019T056. J.H.M is supported by the European Research Council (ERC) advanced grant program (project number 834513) and the Dutch Research Council (NWO) NWA-ORC program (project number 1292.19.077).

Declaration of competing interest

The authors declare that they have no known competing financial interests or personal relationships that could have appeared to influence the work reported in this paper.

Acknowledgments

We thank Petra van der Kraak for her expertise in histopathology, and Francesca Stillitano and Daphne van den Berg for providing access to the Qpath extension. We are grateful to Tom de Boer, Yumeng Wang, Stephan Michel, Tineke Habben-Jansen, Mayke Tersteeg, and Felix Albert for their assistance in the experimental work, and to Esmee Groeneveld for acquiring the echocardiography images. We also thank Maarten-Jan Cramer, Arco Teske, and Saskia de Jager for their valuable scientific input.

Appendix A. Supplementary data

Supplementary data to this article can be found online at https://doi.org/10.1016/j.bbi.2026.106962.

Data availability

Data will be made available on request.

References

Abrahams, H.J.G., Gielissen, M.F.M., Schmits, I.C., Verhagen, C.A.H.H.V.M., Rovers, M. M., Knoop, H., 2016. Risk factors, prevalence, and course of severe fatigue after breast cancer treatment: a meta-analysis involving 12 327 breast cancer survivors. Ann. Oncol. 27 (6), 965–974. https://doi.org/10.1093/annonc/mdw099.

Allen, B.D., Apodaca, L.A., Syage, A.R., et al., 2019. Attenuation of neuroinflammation reverses Adriamycin-induced cognitive impairments. Acta Neuropathol. Commun. 7 (1), 186. https://doi.org/10.1186/s40478-019-0838-8.

Assarsson, E., Lundberg, M., Holmquist, G., et al., 2014. Homogenous 96-Plex PEA immunoassay exhibiting high sensitivity, specificity, and excellent scalability. PLoS One 9 (4), e95192. https://doi.org/10.1371/journal.pone.0095192.

Bankhead, P., Loughrey, M.B., Fernández, J.A., et al., 2017. QuPath: open source software for digital pathology image analysis. Sci. Rep. 7 (1), 16878. https://doi.org/10.1038/s41598-017-17204-5.

Bates, D., Mächler, M., Bolker, B., Walker, S., 2015. Fitting linear mixed-effects models using lme4. J. Stat. Softw. 67, 1–48. https://doi.org/10.18637/jss.v067.i01.

Bayer, A.L., Zambrano, M.A., Smolgovsky, S., et al., 2024. Cytotoxic T cells drive doxorubicin-induced cardiac fibrosis and systolic dysfunction. Nat. Cardiovasc. Res. 3 (8), 970–986. https://doi.org/10.1038/s44161-024-00507-y.

Berger, A.M., Mooney, K., Alvarez-Perez, A., et al., 2015. Cancer-Related Fatigue, Version 2.2015. J. Natl. Compr. Canc. Netw. 13 (8), 1012–1039. https://doi.org/10.6004/jnccn.2015.0122.

Bicker, J., Alves, G., Falcão, A., Fortuna, A., 2020. Timing in drug absorption and disposition: the past, present, and future of chronopharmacokinetics. Br. J. Pharmacol. 177 (10), 2215–2239. https://doi.org/10.1111/bph.15017.

Borniger, J.C., Walker II, W.H., Gaudier-Diaz, M.M., et al., 2017. Time-of-day dictates transcriptional inflammatory responses to cytotoxic chemotherapy. Sci. Rep. 7 (1), 41220. https://doi.org/10.1038/srep41220.

Bouadi O, Yao C, Zeng J, et al. AutoMorFi: Automated Whole-image Morphometry in Fiji/ImageJ for Diverse Image Analysis Needs. bioRxiv. Preprint posted online July 27, 2024:2024.07.26.605357. doi:10.1101/2024.07.26.605357.

Bower, J.E., Ganz, P.A., Irwin, M.R., Arevalo, J.M.G., Cole, S.W., 2011. Fatigue and gene expression in human leukocytes: increased NF-κB and decreased glucocorticoid signaling in breast cancer survivors with persistent fatigue. Brain Behav. Immun. 25 (1), 147–150. https://doi.org/10.1016/j.bbi.2010.09.010.

Bower, J.E., Lamkin, D.M., 2013. Inflammation and cancer-related fatigue: Mechanisms, contributing factors, and treatment implications. Brain Behav. Immun. 30, S48–S57. https://doi.org/10.1016/j.bbi.2012.06.011.

Bray, M.S., Shaw, C.A., Moore, M.W.S., et al., 2008. Disruption of the circadian clock within the cardiomyocyte influences myocardial contractile function, metabolism, and gene expression. Am. J. Phys. Heart Circ. Phys. 294 (2), H1036–H1047. https://doi.org/10.1152/ajpheart.01291.2007.

Cajochen, C., Kräuchi, K., Wirz-Justice, A., 2003. Role of melatonin in the regulation of human circadian rhythms and sleep. J. Neuroendocrinol. 15 (4), 432–437. https://doi.org/10.1046/j.1365-2826.2003.00989.x.

Chou, Y.J., Kober, K.M., Yeh, K.H., et al., 2022. A pilot study of metabolomic pathways associated with fatigue in patients with colorectal cancer receiving chemotherapy. Eur. J. Oncol. Nurs. 56, 102096. https://doi.org/10.1016/j.ejon.2022.102096.

Ciurli, A., Mohammed, Y., Ammon, C., et al., 2024. Spatially and temporally resolved metabolome of the human oral cavity. iScience 27 (2), 108884. https://doi.org/10.1016/j.isci.2024.108884.

Crnko, S., Du Pré, B.C., Sluijter, J.P.G., Van Laake, L.W., 2019. Circadian rhythms and the molecular clock in cardiovascular biology and disease. Nat. Rev. Cardiol. 16 (7), 437–447. https://doi.org/10.1038/s41569-019-0167-4.

de Ligt;, K.M., Heins, M., Verloop, J., Smorenburg, C.H., Korevaar, J.C., Siesling, S., 2019. Patient-reported health problems and healthcare use after treatment for early-stage breast cancer. Breast 46, 4–11. https://doi.org/10.1016/j.breast.2019.03.010.

De Luca A. Use of grip strength meter to assess the limb strength of mdx mice. Published online December 18, 2019. Accessed September 16, 2025. https://www.treat-nmd.org/wp-content/uploads/2023/07/MDX-DMD_M.2.2.001.pdf.

Eyob, T., Ng, T., Chan, R., Chan, A., 2016. Impact of chemotherapy on cancer-related fatigue and cytokines in 1312 patients: a systematic review of quantitative studies. Curr. Opin. Support. Palliat. Care 10 (2), 165. https://doi.org/10.1097/SPC.0000000000000205.

Fabiani, I., Chianca, M., Cipolla, C.M., Cardinale, D.M., 2025. Anthracycline-induced cardiomyopathy: risk prediction, prevention and treatment. Nat. Rev. Cardiol. 22 (8), 551–563. https://doi.org/10.1038/s41569-025-01126-1.

Flanigan, T.J., Anderson, J.E., Elayan, I., Allen, A.R., Ferguson, S.A., 2018. Effects of cyclophosphamide and/or doxorubicin in a murine model of postchemotherapy cognitive impairment. Toxicol. Sci. 162 (2), 462–474. https://doi.org/10.1093/toxsci/kfx267.

Giacchetti, S., Laas, E., Bachelot, T., et al., 2024. Association between endocrine adjuvant therapy intake timing and disease-free survival in patients with high-risk early breast cancer: results of a sub-study of the UCBG- UNIRAD trial. EBioMedicine 104. https://doi.org/10.1016/j.ebiom.2024.105141.

Goedendorp, M.M., Andrykowski, M.A., Donovan, K.A., et al., 2012. Prolonged impact of chemotherapy on fatigue in breast cancer survivors: a longitudinal comparison with radiotherapy-treated breast cancer survivors and noncancer controls. Cancer 118 (15), 3833–3841. https://doi.org/10.1002/cncr.26226.

Grossberg, A.J., Vichaya, E.G., Christian, D.L., et al., 2018. Tumor-associated fatigue in cancer patients develops independently of IL1 signaling. Cancer Res. 78 (3), 695–705. https://doi.org/10.1158/0008-5472.CAN-17-2168.

Grossberg, A.J., Vichaya, E.G., Gross, P.S., et al., 2020. Interleukin 6-independent metabolic reprogramming as a driver of cancer-related fatigue. Brain Behav. Immun. 88, 230–241. https://doi.org/10.1016/j.bbi.2020.05.043.

Hayward, R., Lien, C.Y., Jensen, B.T., Hydock, D.S., Schneider, C.M., 2012. Exercise training mitigates anthracycline-induced chronic cardiotoxicity in a juvenile rat model. Pediatr. Blood Cancer 59 (1), 149–154. https://doi.org/10.1002/pbc.23392.

Hoogland, A.I., Small, B.J., Oswald, L.B., et al., 2023. Relationships among inflammatory biomarkers and self-reported treatment-related symptoms in patients treated with chemotherapy for gynecologic cancer: a controlled comparison. Cancers (Basel) 15 (13), 3407. https://doi.org/10.3390/cancers15133407.

Jemal A, Ward EM, Johnson CJ, et al. Annual Report to the Nation on the Status of Cancer, 1975-2014, Featuring Survival. J Natl Cancer Inst. 2017;109(9):djx030. doi: 10.1093/jnci/djx030.

Jenni, O.G., Deboer, T., Achermann, P., 2006. Development of the 24-h rest-activity pattern in human infants. Infant Behav. Dev. 29 (2), 143–152. https://doi.org/10.1016/j.infbeh.2005.11.001.

Karaboué, A., Innominato, P.F., Wreglesworth, N.I., Duchemann, B., Adam, R., Lévi, F.A., 2024. Why does circadian timing of administration matter for immune checkpoint inhibitors' efficacy? Br. J. Cancer 131 (5), 783–796. https://doi.org/10.1038/s41416-024-02704-9.

Kelters IR, Printezi MI, Ballesta A, et al. Chronotherapy as a novel strategy to limit anthracycline-induced cardiotoxicity. Cardiovascular Research. Published online October 2, 2025. doi:https://doi.org/10.1093/cvr/cvaf179.

Kim, S.M., Neuendorff, N., Earnest, D.J., 2019. Role of proinflammatory cytokines in feedback modulation of circadian clock gene rhythms by saturated fatty acids. Sci. Rep. 9 (1), 8909. https://doi.org/10.1038/s41598-019-45322-9.

Kloosterman, D.J., Erbani, J., Boon, M., et al., 2024. Macrophage-mediated myelin recycling fuels brain cancer malignancy. Cell 187 (19), 5336–5356.e30. https://doi.org/10.1016/j.cell.2024.07.030.

Kuznetsova, A., Brockhoff, P.B., Christensen, R.H.B., 2017. lmerTest package: tests in linear mixed effects models. J. Stat. Softw. 82, 1–26. https://doi.org/10.18637/jss.v082.i13.

Kyriacou, C.P., Hastings, M.H., 2010. Circadian clocks: genes, sleep, and cognition. Trends Cogn. Sci. 14 (6), 259–267. https://doi.org/10.1016/j.tics.2010.03.007.

Laas E, Hamy AS, Bachelot T, et al. Association Between Daily Timing of Everolimus and Survival in High-Risk HR+/HER2- Early Breast Cancer: A Sub-Analysis of the UCBG-UNIRAD Trial. Clin Pharmacol Ther. Published online August 24, 2025. doi: 10.1002/cpt.70030.

Lal, H., Verma, S.K., Wang, Y., Xie, M., Young, M.E., 2024. Circadian Rhythms in Cardiovascular Metabolism. Circ. Res. 134 (6), 635–658. https://doi.org/10.1161/CIRCRESAHA.123.323520.

Lei, Y., VanPortfliet, J.J., Chen, Y.F., et al., 2023. Cooperative sensing of mitochondrial DNA by ZBP1 and cGAS promotes cardiotoxicity. Cell 186 (14), 3013–3032.e22. https://doi.org/10.1016/j.cell.2023.05.039.

Lenth RV. emmeans: Estimated Marginal Means, aka Least-Squares Means. R package version 1.11.2-80001. Published online 2025. https://rvlenth.github.io/emmeans/.

Lévi, F.A., Okyar, A., Hadadi, E., Innominato, P.F., Ballesta, A., 2024. Circadian regulation of drug responses: toward sex-specific and personalized chronotherapy. Annu. Rev. Pharmacol. Toxicol. 64, 89–114. https://doi.org/10.1146/annurev-pharmtox-051920-095416.

Loman, B.R., Jordan, K.R., Haynes, B., Bailey, M.T., Pyter, L.M., 2019. Chemotherapy-induced neuroinflammation is associated with disrupted colonic and bacterial homeostasis in female mice. Sci. Rep. 9 (1), 16490. https://doi.org/10.1038/s41598-019-52893-0.

Ma, Y., He, B., Jiang, M., et al., 2020. Prevalence and risk factors of cancer-related fatigue: a systematic review and meta-analysis. Int. J. Nurs. Stud. 111, 103707. https://doi.org/10.1016/j.ijnurstu.2020.103707.

Mahoney, S.E., Davis, J.M., Murphy, E.A., McClellan, J.L., Gordon, B., Pena, M.M., 2013. Effects of 5-fluorouracil chemotherapy on fatigue: role of MCP-1. Brain Behav. Immun. 27 (1), 155–161. https://doi.org/10.1016/j.bbi.2012.10.012.

Naviaux, R.K., Naviaux, J.C., Li, K., et al., 2016. Metabolic features of chronic fatigue syndrome. Proc. Natl. Acad. Sci. 113 (37), E5472–E5480. https://doi.org/10.1073/pnas.1607571113.

Panda, S., 2016. Circadian physiology of metabolism. Science 354 (6315), 1008–1015. https://doi.org/10.1126/science.aah4967.

Pang, Z., Lu, Y., Zhou, G., et al., 2024. MetaboAnalyst 6.0: towards a unified platform for metabolomics data processing, analysis and interpretation. Nucleic Acids Res. 52 (W1), W398–W406. https://doi.org/10.1093/nar/gkae253.

Pang, B., Qiao, X., Janssen, L., et al., 2013. Drug-induced histone eviction from open chromatin contributes to the chemotherapeutic effects of doxorubicin. Nat. Commun. 4 (1), 1908. https://doi.org/10.1038/ncomms2921.

Patke, A., Young, M.W., Axelrod, S., 2020. Molecular mechanisms and physiological importance of circadian rhythms. Nat. Rev. Mol. Cell Biol. 21 (2), 67–84. https://doi.org/10.1038/s41580-019-0179-2.

Printezi, M.I., Teske, A.J., Zuithoff, N.P.A., et al., 2025. Morning administration of anthracyclines is associated with a lower risk of cancer therapy-related cardiac dysfunction. Eur Heart J Open 5 (5), oeaf100. https://doi.org/10.1093/ehjopen/oeaf100.

Qiao, X., van der Zanden, S.Y., Wander, D.P.A., et al., 2020. Uncoupling DNA damage from chromatin damage to detoxify doxorubicin. Proc. Natl. Acad. Sci. 117 (26), 15182–15192. https://doi.org/10.1073/pnas.1922072117.

R Core Team. R: A Language and Environment for Statistical Computing. Published online 2024. https://www.R-project.org/.

Rendeiro, C., Sheriff, A., Bhattacharya, T.K., et al., 2016. Long-lasting impairments in adult neurogenesis, spatial learning and memory from a standard chemotherapy regimen used to treat breast cancer. Behav. Brain Res. 315, 10–22. https://doi.org/10.1016/j.bbr.2016.07.043.

Rosensweig, C., Green, C.B., 2020. Periodicity, repression, and the molecular architecture of the mammalian circadian clock. Eur. J. Neurosci. 51 (1), 139–165. https://doi.org/10.1111/ejn.14254.

Santos, J.C., Pyter, L.M., 2018. Neuroimmunology of behavioral comorbidities associated with cancer and cancer treatments. Front. Immunol. 9. https://doi.org/10.3389/fimmu.2018.01195.

Scheiermann, C., Kunisaki, Y., Frenette, P.S., 2013. Circadian control of the immune system. Nat. Rev. Immunol. 13 (3), 190–198. https://doi.org/10.1038/nri3386.

Schibler, U., Gotic, I., Saini, C., et al., 2015. Clock-talk: interactions between central and peripheral circadian oscillators in mammals. Cold Spring Harb. Symp. Quant. Biol. 80, 223–232. https://doi.org/10.1101/sqb.2015.80.027490.

Scott, K., Phan, T.T., West, A.P., Taniguchi, C.M., Dantzer, R., 2022. Neutralizing interleukin-6 in tumor-bearing mice does not abrogate behavioral fatigue induced by Lewis lung carcinoma. Behav. Brain Res. 417, 113607. https://doi.org/10.1016/j.bbr.2021.113607.

Singh, S., Giron, L.B., Shaikh, M.W., et al., 2024. Distinct intestinal microbial signatures linked to accelerated systemic and intestinal biological aging. Microbiome 12 (1), 31. https://doi.org/10.1186/s40168-024-01758-4.

Stone, P., Richardson, A., Ream, E., Smith, A.G., Kerr, D.J., Kearney, N., 2000. Cancer-related fatigue: inevitable, unimportant and untreatable? Results of a multi-centre patient survey. Cancer Fatigue Forum. Ann Oncol. 11 (8), 971–975. https://doi.org/10.1023/a:1008318932641.

Sullivan, K.A., Grant, C.V., Jordan, K.R., Obrietan, K., Pyter, L.M., 2022. Paclitaxel chemotherapy disrupts behavioral and molecular circadian clocks in mice. Brain Behav. Immun. 99, 106–118. https://doi.org/10.1016/j.bbi.2021.09.011.

Tapp, Z.M., Ghosh, A.K., Obrietan, K.H., Pyter, L.M., 2025. Mechanistic insights into chemotherapy-induced circadian disruption using rodent models. Trends Neurosci. 48 (4), 283–296. https://doi.org/10.1016/j.tins.2024.12.011.

Teleanu, R.I., Niculescu, A.G., Roza, E., Vladâcenco, O., Grumezescu, A.M., Teleanu, D. M., 2022. Neurotransmitters-key factors in neurological and neurodegenerative disorders of the central nervous system. Int. J. Mol. Sci. 23 (11), 5954. https://doi.org/10.3390/ijms23115954.

Tewey, K.M., Rowe, T.C., Yang, L., Halligan, B.D., Liu, L.F., 1984. Adriamycin-induced DNA damage mediated by mammalian DNA topoisomerase II. Science 226 (4673), 466–468. https://doi.org/10.1126/science.6093249.

Thong, M.S.Y., van Noorden, C.J.F., Steindorf, K., Arndt, V., 2020. Cancer-related fatigue: causes and current treatment options. Curr Treat Options Oncol. 21 (2), 17. https://doi.org/10.1007/s11864-020-0707-5.

Tometich, D.B., Hoogland, A.I., Small, B.J., et al., 2023. Relationships among inflammatory biomarkers and objectively assessed physical activity and sleep during and after chemotherapy for gynecologic malignancies. Cancers (Basel) 15 (15), 3882. https://doi.org/10.3390/cancers15153882.

van der Geest, J.S.A., Kelters, I.R., Arends, B., et al., 2025. Dexrazoxane protects against doxorubicin-induced cardiotoxicity in susceptible human living myocardial slices: a proof-of-concept study. Br. J. Pharmacol. 182 (18), 4262–4280. https://doi.org/10.1111/bph.70085.

van Eenige, R., Verhave, P.S., Koemans, P.J., Tiebosch, I.A.C.W., Rensen, P.C.N., Kooijman, S., 2020. RandoMice, a novel, user-friendly randomization tool in animal research. PLoS One 15 (8), e0237096. https://doi.org/10.1371/journal.pone.0237096.

van Roekel, E.H., Bours, M.J.L., Breukink, S.O., et al., 2023. Longitudinal associations of plasma metabolites with persistent fatigue among colorectal cancer survivors up to 2 years after treatment. Int. J. Cancer 152 (2), 214–226. https://doi.org/10.1002/ijc.34252.

Wang, J., Liu, S., Meng, X., et al., 2024. Exercise Inhibits Doxorubicin-Induced Cardiotoxicity via Regulating B Cells. Circ. Res. 134 (5), 550–568. https://doi.org/10.1161/CIRCRESAHA.123.323346.

Wang, C., Lutes, L.K., Barnoud, C., Scheiermann, C., 2022. The circadian immune system. Sci. Immunol. 7 (72), eabm2465. https://doi.org/10.1126/sciimmunol.abm2465.

Wang, Y., van der Zanden, S.Y., van Leerdam, S., et al., 2022. Induction of fatigue by specific anthracycline cancer drugs through disruption of the circadian pacemaker. Cancers 14 (10), 2421. https://doi.org/10.3390/cancers14102421.

Wang, Y., van Beurden, A.W., Tersteeg, M.M.H., et al., 2024. Internal circadian misallignment in a mouse model of chemotherapy induced fatigue. Brain Behav. Immun. 115, 588–599. https://doi.org/10.1016/j.bbi.2023.11.020.

Wefel, J.S., Kesler, S.R., Noll, K.R., Schagen, S.B., 2015. Clinical characteristics, pathophysiology, and management of noncentral nervous system cancer-related cognitive impairment in adults. CA Cancer J. Clin. 65 (2), 123–138. https://doi.org/10.3322/caac.21258.

Weymann, K.B., Wood, L.J., Zhu, X., Marks, D.L., 2014. A role for orexin in cytotoxic chemotherapy-induced fatigue. Brain Behav. Immun. 37, 84–94. https://doi.org/10.1016/j.bbi.2013.11.003.

Wood, L.J., Nail, L.M., Perrin, N.A., Elsea, C.R., Fischer, A., Druker, B.J., 2006. The cancer chemotherapy drug etoposide (VP-16) induces proinflammatory cytokine production and sickness behavior-like symptoms in a mouse model of cancer chemotherapy-related symptoms. Biol. Res. Nurs. 8 (2), 157–169. https://doi.org/10.1177/1099800406290932.

Zombeck, J.A., Fey, E.G., Lyng, G.D., Sonis, S.T., 2013. A clinically translatable mouse model for chemotherapy-related fatigue. Comp. Med. 63 (6), 491–497.